ADVANCED MATERIALS INTERFACES

Supporting Information

A Long-Overlooked Pitfall in Rechargeable Zinc–Air Batteries: Proper Electrode Balancing

Daniel Deckenbach and Jörg J. Schneider*

Supporting Information

A long-overlooked pitfall in rechargeable zinc-air batteries: Proper electrode balancing

Daniel Deckenbach, and Jörg J. Schneider*

Additional information on the depth of discharge

The depth of discharge is one of the most sensitive parameters to increase the specific energy of zinc-air batteries. However, a simple increase in DoD is difficult due to the well-known correlation of a shortened cycle life with increased depth of discharge.[1] A decisive hurdle is posed by the self-limitation of classical zinc metal anodes, usually caused by passivation, which autonomously interrupts the discharge process even though the zinc reservoir has not yet been completely utilized. Therefore, the DoD can be used as a measure to evaluate the self-limitation of classical zinc metal anodes in order to draw a conclusion about the reversibility and thus also the rechargeability. The classification of the depth of discharge within this investigation focuses on the two borderline cases of a low and high DoD, with the upper limit of the low DoD and the lower limit of the high DoD defined on the basis of the self-limitation of the zinc metal anode. In the case of the high DoD anode, self-limitation is achieved by a simple discharge until no further oxidation is possible. This procedure formally corresponds to the operation of a primary cell, which represents a benchmark for the development of deep-dischargeable zinc anodes. Since it should be worthwhile for a rechargeable zinc-air battery to provide at least the same specific energy as the non-rechargeable counterpart, it represents the lower limit for high DoD anodes. The determination of the upper limit of the low DoD of classical zinc metal anodes is carried out analogously considering the self-limitation of the zinc anode but by means of cyclisation instead of a single discharge. To ensure a valid level of comparability, an assumption is made according to which the time until self-limitation of the zinc anode is reached should be the same for operation under low and high DoD, so that further external influences i.e. catalyst failure that endanger a comparison in the context of the full-cell investigation are minimized. The experimental determination of the low and high DoD limits was carried out performing full cell testing with a classical zinc metal anode (100 µm thickness) against a benchmark

Pt/C-Ir/C-catalyst in standardized 6M KOH electrolyte until the self-limitation of the zinc anode has been attained (Figure S 1).
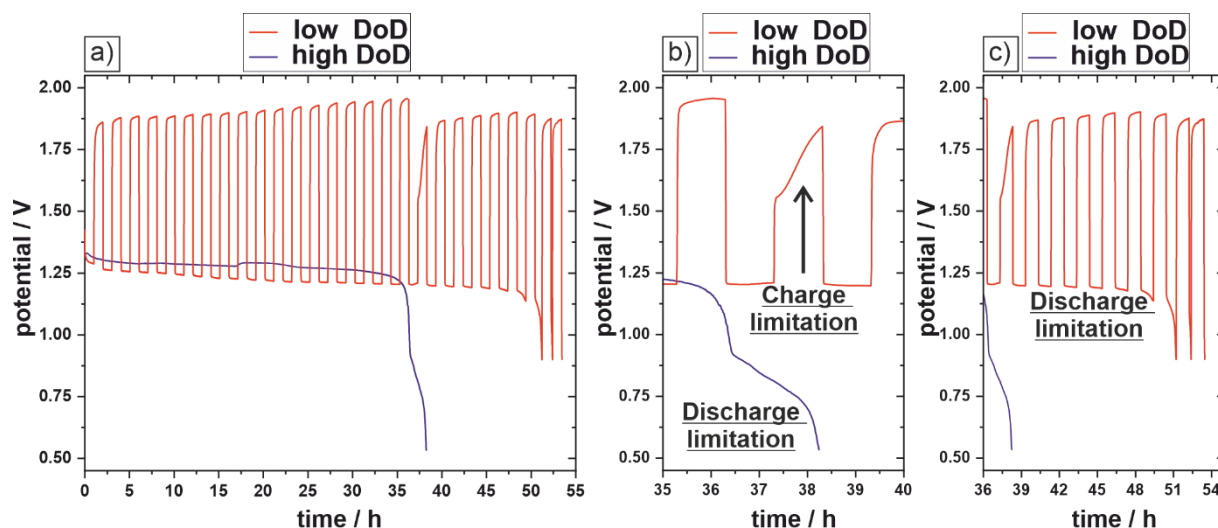

Figure S 1: Full-cell investigation on classical zinc metal anodes for the classification of suitable regimes for low and high DoD. The lower limit of the high DoD is defined by the maximum specific energy that can be extracted from a single discharge, in which a threshold value of 42 % could be determined. Based on the assumption that self-limitation of the low DoD zinc anode should occur in the same time interval for better comparability, the upper limit of the low DoD anode was set to a threshold value of one percent. Both the low and high DoD anodes reached self-limitation within about 38 hours in this evaluation (a). The high DoD anode exhibits a discharge limitation, whereas the low DoD anode initially develops a charge limitation (b) until after subsequent seven discharge-charge cycles the discharge limitation also appears (c). (b) is an enlarged section of (a) in the time interval of 25 – 40 hours while (c) highlights the time interval of 36 – 55 hours.

In high DoD mode, the zinc anode is discharged over a period of about 38 hours, reaching a depth of discharge of 42 % until the self-limitation of the anode stops the discharge. The obtained DoD at single discharge is in good agreement with ready-to-buy Zn-air cells with typical DoD values below 50 % marking the lower end of high DoD.[2,3] At a depth of discharge of one percent, the self-limitation in the low DoD mode is reached in a comparable time as with single discharge in the high DoD mode, so that any effects on the part of the cathode i.e. the catalyst can be neglected. In contrast to the high DoD mode, the low DoD anode initially exhibits a limitation of the charging process, which is evident from a voltage drop in the charging plateau of 100 mV for the subsequent seven cycles (Figure S 1 b). Following this voltage decline, the low DoD anode also runs into the self-limitation of the discharge process. Since the self-limitation was reached in the low DoD mode, this represents the upper limit of the low DoD and below this, the influence of the anode degradation on the cycle life is steadily reduced as the depth of discharge decreases.
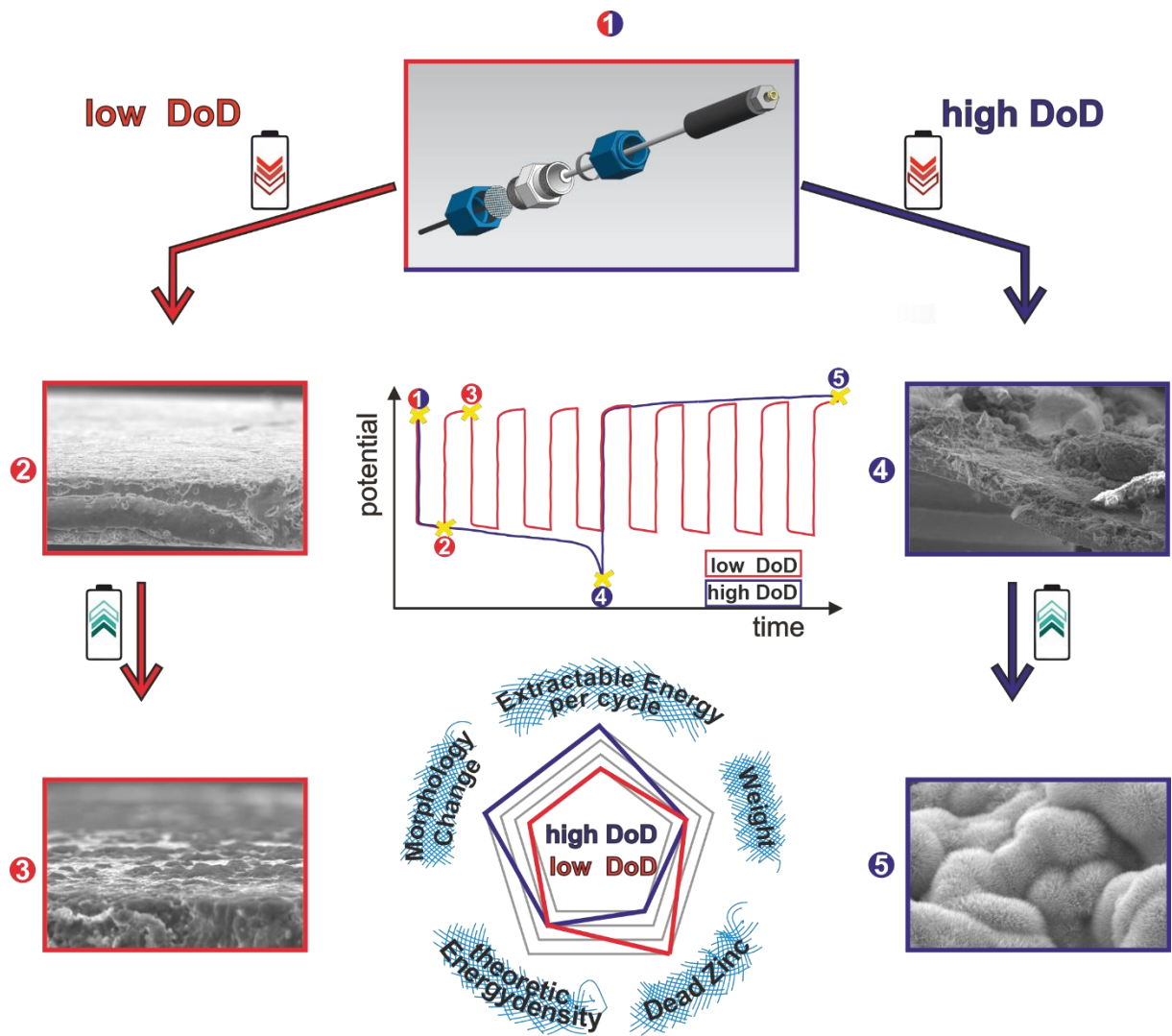
Figure S 2: Experimental counterparts of the situation of zinc anodes under shallow and deep discharge (see Figure 2 for the schematic presentation) under real conditions in a zinc-air battery. SEM image size is ~100 μm per cm.
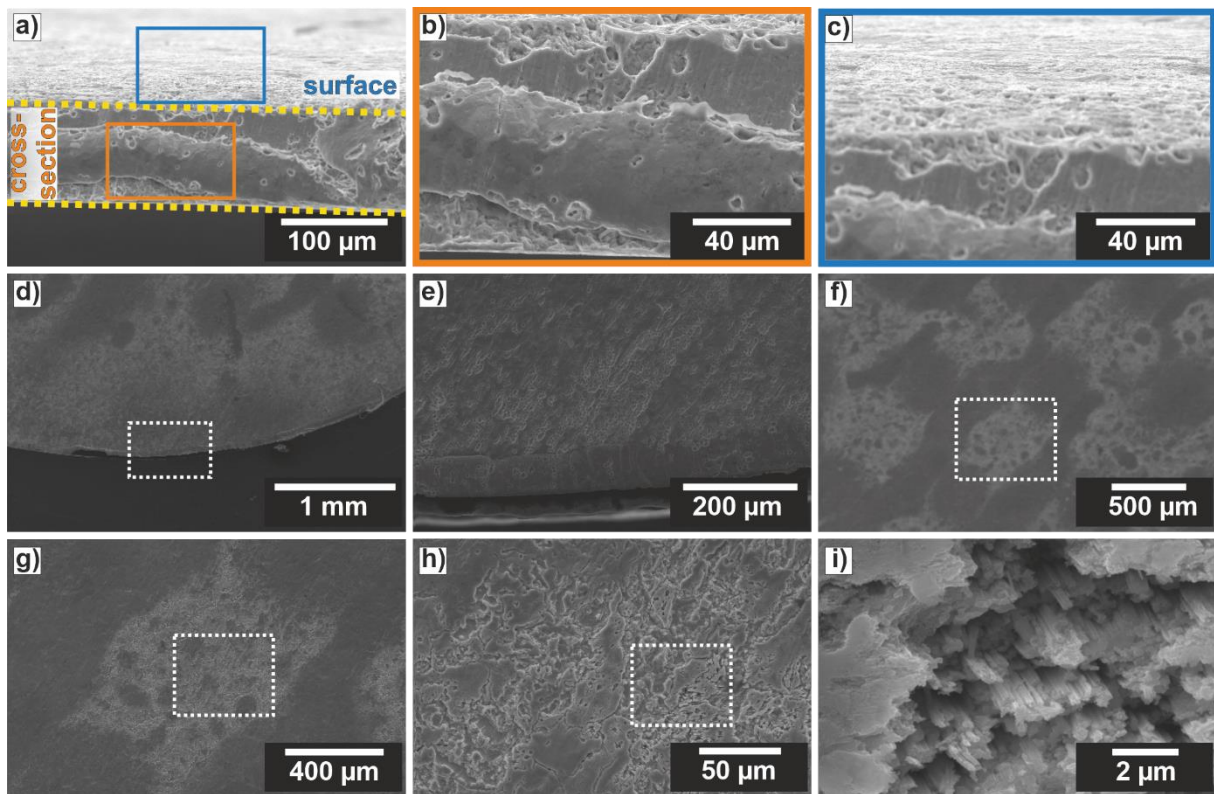
Figure S 3: Post-mortem SEM-analysis of a zinc anode with 100 µm thickness after a single discharge in a real zinc-air battery at a low DoD of one percent. After a single discharge at low DoD, the zinc anode is only slightly affected. The cross-section shows no significant change in thickness (a). Due to the discharge, the zinc anode shows holes caused by the attack of the KOH electrolyte (b, c). The edge of the zinc anode is unchanged and shows a round shape as cut out (d, e). (e) is a higher magnification image of (d). The surface of the zinc anode is roughened and appears etched, but overall only minor surface changes are visible (f-i) The patterned surface is caused by the contact with the separator during discharge (f). Within the image sequence (f) to (i) the magnification increases continuously.
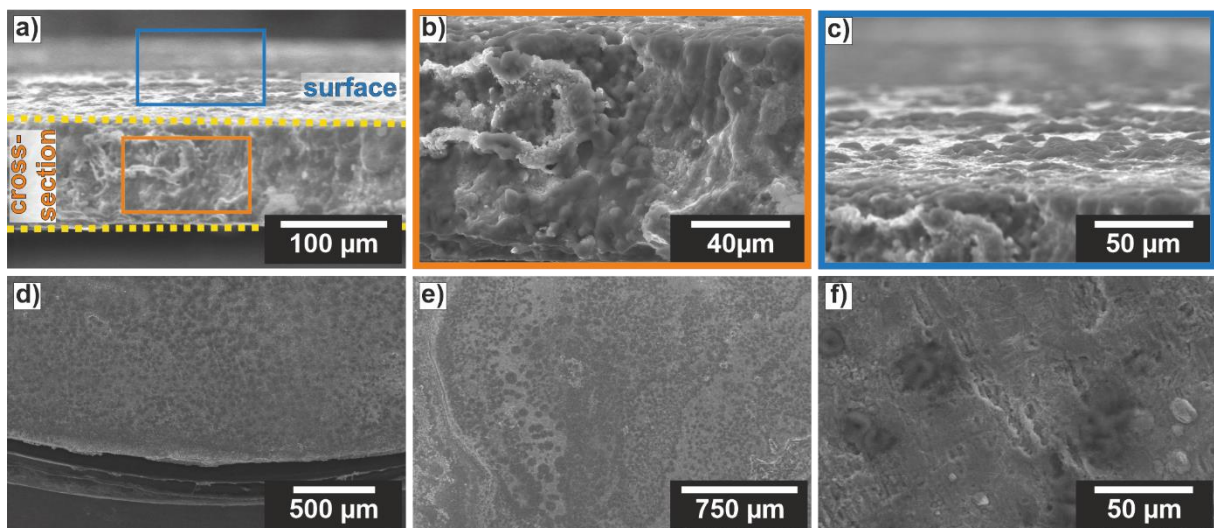

Figure S 4: Post-mortem SEM-analysis of a zinc anode with 100 µm thickness after a single discharge-charge sequence in a real zinc-air battery at a low DoD of one percent. After charging and discharging the zinc anode once, the cross-section still shows a homogeneous zinc metal electrode (a-c). Due to the charging of the cell, the previously generated holes during discharge are filled up by the zinc deposition process taking place. The anode surface is smoothed and only minor deposits on the electrode surface are visible (d-f).
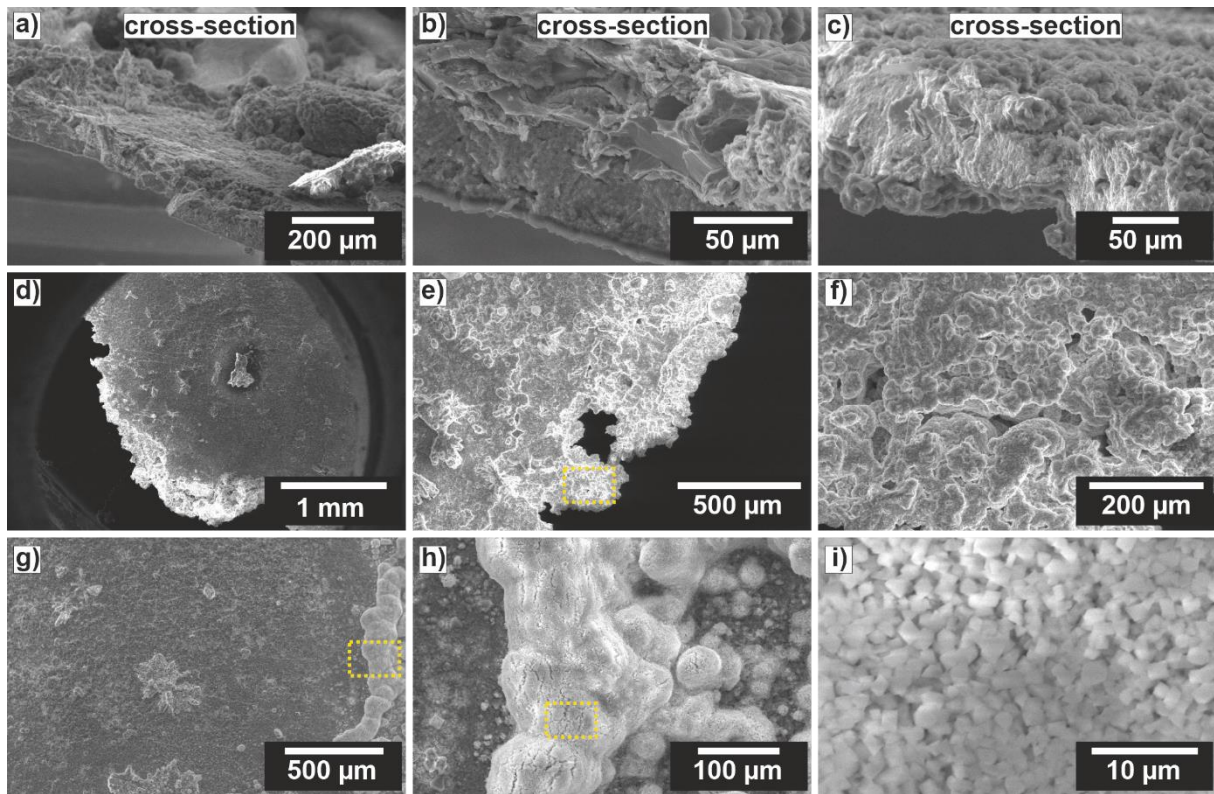
Figure S 5: Post-mortem SEM-analysis of a zinc anode with 100 µm thickness after a single discharge in a real zinc-air battery at a high DoD of 42 %. The cross-section of the zinc anode at high DoD reveals the massive morphological change (a). Due to the high DoD an intertwined interface (b) and a passivation (c) is observed. During discharge a lot of the zinc is dissolved within the electrolyte reducing the active zinc mass, which leads to a reduction of the electrode geometry. The electrode edges appear fringed (d) and holey (e). (f) is a higher magnification of (e) showing the generated void space during deep discharge. At high DoD the surface of the zinc anode is no more homogeneous, and a white deposit is visible, which is primarily composed of oxidized zinc species showing a cuboid morphology. Within the image-sequence (g) to (i) the magnification increases steadily.
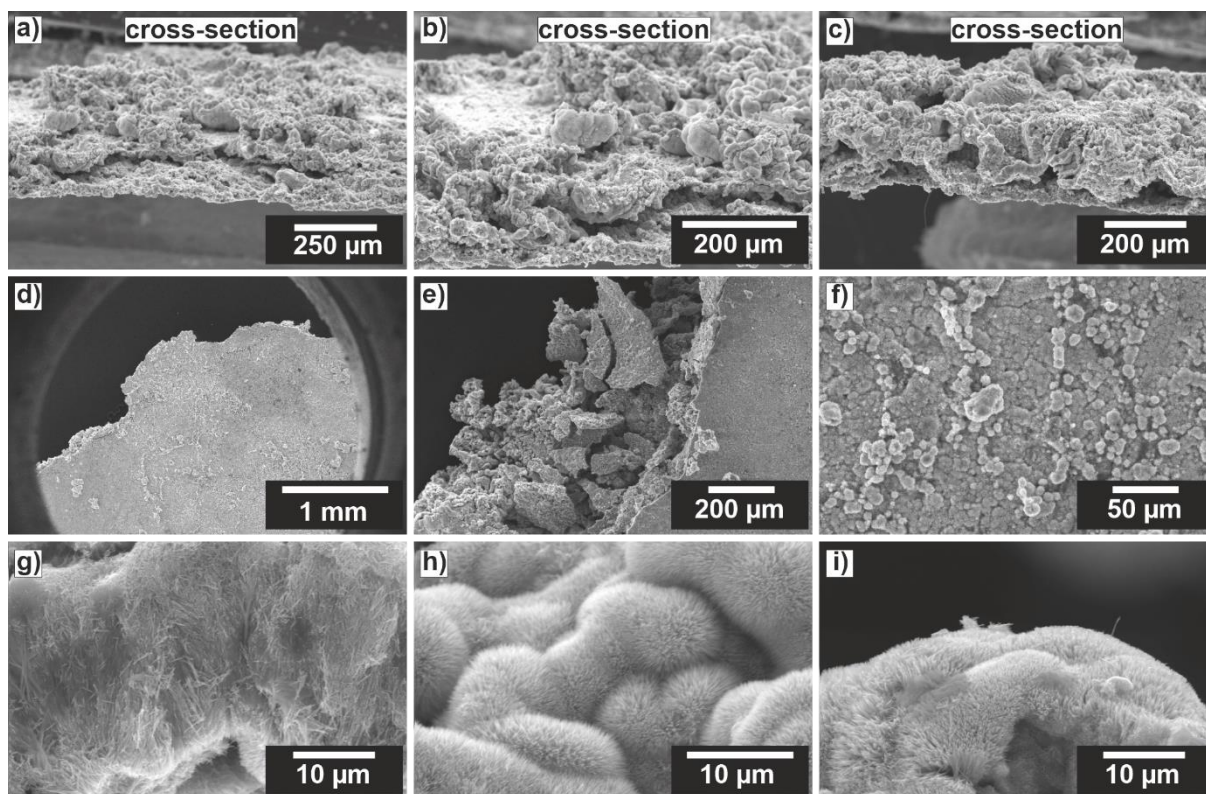
Figure S 6: Post-mortem SEM-analysis of a zinc anode with 100 µm thickness after a discharge-charge sequence in a real zinc-air battery at a high DoD of 42 %. After charging the deeply discharged zinc anode, the cross-section still shows a very inhomogeneous distribution of the zinc species (a, b). Compared to the low DoD anode, the charge step does not smoothen the surface (c). The charging step also does not compensate for the zinc loss during discharge, so the electrode edge is still fringed (d) and brittle (e). The fragility of the electrode shows the development of an intertwined Zn/ZnO-interface. The surface of the zinc anode is irregular showing well developed dendrite formation (g-i).
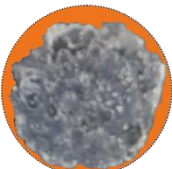
a) zinc anode 100 µm; 12mm — pristine
- non-polished, metallic surface
- circular shape
- sharp edges

b) zinc anode 100 µm; 12mm — low DoD Discharge
- patterned, metallic surface
- negative replica of separator
- circular shape
- sharp edges
- no shape change

c) zinc anode 100 µm; 12mm — low DoD Discharge-Charge
- patterned, discoloured surface
- minor deformation of circular shape
- marginal loss of zinc

d) zinc anode 100 µm; 12mm — high DoD Discharge
- white, oxidised surface
- passivation layer
- obvious deformation of circular shape
- significant loss of zinc

e) zinc anode 100 µm; 12mm — high DoD Discharge-Charge
- zinc-coloured, inhomogeneous surface
- manifold grain boundaries
- intertwined interface
- deformation of circular shape

f) zinc anode 100 µm; 12mm — high DoD Discharge
backside -coin cell-
- white, oxidised surface
- passivation layer
- loss of electrical contact

Figure S 7: Corresponding optical images of the zinc anodes operated under high and low DoD in discharge and discharge-charge experiments. A single shallow discharge does not change the electrode geometry compared to a pristine zinc anode (a), only a pattern caused by the separator is visible on the electrode surface (b). Charging the low DoD anode leads to a discoloration of the metallic electrode (c). The electrode geometry is preserved, only a marginal loss of zinc is visible. A deeply discharged zinc anode shows massive ZnO formation on the surface, representing a passivation layer. A deformation of the circular electrode shape is discernible, accompanied with a significant loss of zinc (d). When a deeply discharged zinc anode is charged again, the electrode surface appears zinc-colored due to the deposition process taking place. An inhomogeneous discoloration of the electrode surface indicates grain boundaries and a further intertwined interface. A still present deformation of the circular electrode shape depicts that the charging step is insufficient to cope with the zinc loss (e). When a zinc anode is operated in a cell, where the electrolyte can assess the backside of the electrode, as in coin cells, a formation of a passivation is obvious, prohibiting further electron conduction (f).

Table S 1: Basic principles for the design of zinc electrodes and electrolytes based on Zhang[4] et al.[5–27]

categorie			principle	type	description	material	Source
z i n c e l e c t r o d e	I n t e r f a c e	concentration field	size exclusion	buffer layer	channels to mechanically change concentration field	Nafion-Zn-X	[5]
			electronic interaction	organic	donate electron pairs to guide coordination adsorbtion	polyamide	[6]
				inorganic	directional polarization field induces orderded Zn^{2+} migration	$BaTiO_3$	[7]
		Electric field	Homogenizing of Electric field	modify conductive layer	suppression of 2D diffusion of Zn^{2+}	Carbon	[8]
						Mxene	[9]
			Enlarging local electric field	constructing protrusions	strengthen the 2D diffusion	Au-Particles	[10]
		surface energy	zincophilic sites	zinc affinity	N-containing sites change the Zn affinity of graphene	N-doped graphene	[11]
			Exposing single facet		lower Zn affinity of crystal facet repels Zn adsorption	(001),(101) TiO2	[12]
	Structural anode		3D	metals	3D design increses Zn nucelation sites	Cu-foam	[13]
				carbonaceous		Carbon nanotubes	[14]
			2D	carbonaceous	atomic arrangement locks the crystal orientation relationship	Graphene	[15]
	Alloying anode		solid alloy	solid-solution reaction	improve corrosion resistance	Cu-Zn	[16]
						Ag-Zn	[17]
			liquid alloy	self-healing	accumulation of excess zinc under alloy layer	Ga-In-Zn	[18]
			more active zinc alloys	passivation	uniform Zn deposition by constructing an insulating frame	$Zn_{88}Al_{12}$	[19]
Electrolyte			Weakening of solvation effect	species	reduces number of water molecules in solvent sheath	$Zn(OTf)_2$	[20]
				concentration	high concentration reduces water activity	$ZnCl_2$	[21]
				additives	enter the primary solvation shell	Glucose	[22]
					antisolvent attract free water molecules from solvation of Zn^{2+}	Methanol	[23]
			suppression of 2D diffusion	physical barrier	organic additivs on a surface of Zn anode inhibit Zn^{2+}-2D diffusion	Glycerol	[24]
				adsorbtion of Zn^{2+}		Arginin	[25]
			electrostatic shielding layer	electrostatic	counteracting tip effect	TBA_2SO_4	[26]
			in-situ SEI	electrolyte decomposition	ZnF_2- rich inner layer enhances desolvation,	$Me_3EtNOTF)$	[27]

Materials: Two different zinc anodes were used to perform zinc-air battery measurements. A zinc metal anode with a thickness of 100 μm (Chempur, 99,99 %+) was commercially purchased, whereas a zinc anode with a thickness of 1 μm was prepared in-house by thermal deposition of zinc (Alfa Aesar, 99 % metals basis) on a current collector (tin, Sn, EppsteinFoils, 99 %). Thermal deposition was performed at a HHV Auto 306, equipped with a FL400 chamber and an Infineon SQM 160 microbalance. During the deposition process the pressure was kept at $5 \cdot 10^{-5}$ mbar with a deposition rate of 5 Å/s while the sample was mounted on a rotary work holder to ensure a homogeneous film thickness. The catalysts used were commercially sourced to provide comparability: Pt/C-catalyst (HiSpec® 3000, Alfa Aesar, 20 % platinum on carbon black) and Ir/C-catalyst (FC Catalyst, FuelCell Store, 20 % iridium on Vulcan XC-72), activated carbon catalyst (CNH, carbon nanohorns TIE GmbH, Griesheim). Catalysts were coated on gas diffusion electrodes (Sigracet®, SGL, 39BB) with a catalyst mass loading of 1.5 mg/cm² employing Nafion (5 % in water/isopropanol, D520, Alfa Aesar) as binder. Two different electrolytes were investigated: the alkaline, aqueous KOH electrolyte (6M, Bernd Kraft) and the aqueous zinc triflate electrolyte (1M, 98 %, ABCR in H_2O, HPLC gradient grade, Carl Roth).

Electrochemical Characterization: An in-house manufactured two electrode test cell[28] was employed for subsequent electrochemical characterization. Details are reproduced here: A Swagelok® connector (PFA/ASTM D3307 Type I) as cell casing, a cylindrical, perforated metal plate equipped with a pin electrode (20 mm plate diameter, 50 mm pin length, stainless steel, AISI316) as

cathode current collector and a fully tin stamp electrode (13 mm diameter, 100 mm shaft length, Sn, 99,9 %) mounted in a guide holder (13 mm diameter, 55 mm length, 5 mm bore, fiber-glass-reinforced polyamide 6.6) as current collector on anode side. The cell assembly requires an adhesive connection (3M VHB tape 4905) to mount the gas diffusion electrode directly onto the Swagelok® connector with the catalyst layer facing the internal part of the cell case. The stainless-steel current collector on cathode side is seized by a screw cap. The catalyst layer is separated by two cylindrical laminated separator discs (14 mm diameter, 110 µm thickness, surfactant coated, Celgard® 5550) from the zinc anode on the anode side. The zinc anode is completely immersed in the electrolyte volume (1 mL), whereby the zinc anode is fixed on the tin stamp electrode by means of silver conductive paint. The electrochemical evaluation was performed using a VMP3 multichannel potentiostat (Bio-Logic). Galvanostatic discharge profiles of zinc-air cells were recorded referring to current literature at 0.5 mA/cm^2.[29] All the electrochemical tests were conducted at 25 °C. The depth of discharge is calculated according to PARKER et. al. on the basis of the theoretic capacity of zinc (819 mAh/g) and the total mass of the zinc anode.[30]
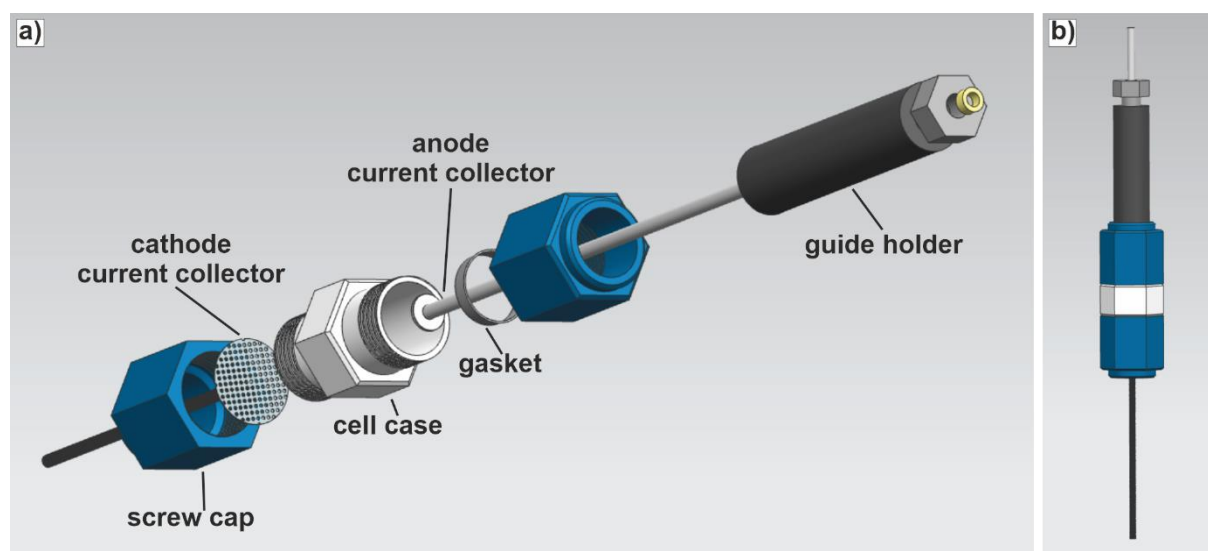

Figure S 8: Two electrode zinc-air test cell for investigation of rechargeability in exploded view (a) and assembled view (b).[28]

References:

[1]   B. J. Hopkins, C. N. Chervin, J. W. Long, D. R. Rolison, J. F. Parker, *ACS Energy Lett.* **2020**, *5*, 3405.

[2]   H. Luo, B. Liu, Z. Yang, Y. Wan, C. Zhong, *Electrochem. Energ. Rev.* **2022**, *5*, 187.

[3]   Y. Li, J. Lu, *ACS Energy Lett.* **2017**, *2*, 1370.

[4]   J. Yang, B. Yin, Y. Sun, H. Pan, W. Sun, B. Jia, S. Zhang, T. Ma, *Nano-micro letters* **2022**, *14*, 42.

[5] S.-B. Wang, Q. Ran, R.-Q. Yao, H. Shi, Z. Wen, M. Zhao, X.-Y. Lang, Q. Jiang, *Nature communications* **2020**, *11*, 1634.

[6] C. Zhang, J. Holoubek, X. Wu, A. Daniyar, L. Zhu, C. Chen, D. P. Leonard, I. A. Rodríguez-Pérez, J.-X. Jiang, C. Fang, X. Ji, *Chemical communications (Cambridge, England)* **2018**, *54*, 14097.

[7] C. Liu, Z. Luo, W. Deng, W. Wei, L. Chen, A. Pan, J. Ma, C. Wang, L. Zhu, L. Xie, X.-Y. Cao, J. Hu, G. Zou, H. Hou, X. Ji, *ACS Energy Lett.* **2021**, *6*, 675.

[8] Z. Cai, Y. Ou, J. Wang, R. Xiao, L. Fu, Z. Yuan, R. Zhan, Y. Sun, *Energy Storage Materials* **2020**, *27*, 205.

[9] Y. Wang, Y. Chen, W. Liu, X. Ni, P. Qing, Q. Zhao, W. Wei, X. Ji, J. Ma, L. Chen, *J. Mater. Chem. A* **2021**, *9*, 8452.

[10] H. Lu, X. Zhang, M. Luo, K. Cao, Y. Lu, B. B. Xu, H. Pan, K. Tao, Y. Jiang, *Adv. Funct. Mater.* **2021**, *31*, 2103514.

[11] A. Bayaguud, X. Luo, Y. Fu, C. Zhu, *ACS Energy Lett.* **2020**, *5*, 3012.

[12] Y. Zhang, M. Zhu, K. Wu, F. Yu, G. Wang, G. Xu, M. Wu, H.-K. Liu, S.-X. Dou, C. Wu, *J. Mater. Chem. A* **2021**, *9*, 4253.

[13] P. Sun, L. Ma, W. Zhou, M. Qiu, Z. Wang, D. Chao, W. Mai, *Angewandte Chemie (International ed. in English)* **2021**, *60*, 18247.

[14] J. Hao, L. Yuan, C. Ye, D. Chao, K. Davey, Z. Guo, S.-Z. Qiao, *Angewandte Chemie (International ed. in English)* **2021**, *60*, 7366.

[15] J. Zheng, Q. Zhao, T. Tang, J. Yin, C. D. Quilty, G. D. Renderos, X. Liu, Y. Deng, L. Wang, D. C. Bock, C. Jaye, D. Zhang, E. S. Takeuchi, K. J. Takeuchi, A. C. Marschilok, L. A. Archer, *Science (New York, N.Y.)* **2019**, *366*, 645.

[16] L. Dong, W. Yang, W. Yang, H. Tian, Y. Huang, X. Wang, C. Xu, C. Wang, F. Kang, G. Wang, *Chemical Engineering Journal* **2020**, *384*, 123355.

[17] N. Zhang, S. Huang, Z. Yuan, J. Zhu, Z. Zhao, Z. Niu, *Angewandte Chemie (International ed. in English)* **2021**, *60*, 2861.

[18] K. Wu, J. Yi, X. Liu, Y. Sun, J. Cui, Y. Xie, Y. Liu, Y. Xia, J. Zhang, *Nano-micro letters* **2021**, *13*, 79.

[19] Y. Cui, Q. Zhao, X. Wu, X. Chen, J. Yang, Y. Wang, R. Qin, S. Ding, Y. Song, J. Wu, K. Yang, Z. Wang, Z. Mei, Z. Song, H. Wu, Z. Jiang, G. Qian, L. Yang, F. Pan, *Angewandte Chemie (International ed. in English)* **2020**, *59*, 16594.

[20] Z. Zhao, J. Zhao, Z. Hu, J. Li, J. Li, Y. Zhang, C. Wang, G. Cui, *Energy Environ. Sci.* **2019**, *12*, 1938.

[21] M. Cui, Y. Xiao, L. Kang, W. Du, Y. Gao, X. Sun, Y. Zhou, X. Li, H. Li, F. Jiang, C. Zhi, *ACS Appl. Energy Mater.* **2019**, *2*, 6490.

[22] Y. Zeng, X. Zhang, R. Qin, X. Liu, P. Fang, D. Zheng, Y. Tong, X. Lu, *Advanced materials (Deerfield Beach, Fla.)* **2019**, *31*, e1903675.

[23] X. Shi, G. Xu, S. Liang, C. Li, S. Guo, X. Xie, X. Ma, J. Zhou, *ACS Sustainable Chem. Eng.* **2019**, *7*, 17737.

[24] Q. Zhang, J. Luan, X. Huang, Q. Wang, D. Sun, Y. Tang, X. Ji, H. Wang, *Nature communications* **2020**, *11*, 3961.

[25] F. Xie, H. Li, X. Wang, X. Zhi, D. Chao, K. Davey, S.‑Z. Qiao, *Adv. Energy Mater.* **2021**, *11*, 2003419.

[26] L. Cao, D. Li, T. Pollard, T. Deng, B. Zhang, C. Yang, L. Chen, J. Vatamanu, E. Hu, M. J. Hourwitz, L. Ma, M. Ding, Q. Li, S. Hou, K. Gaskell, J. T. Fourkas, X.-Q. Yang, K. Xu, O. Borodin, C. Wang, *Nature nanotechnology* **2021**, *16*, 902.

[27] N. Zhang, F. Cheng, Y. Liu, Q. Zhao, K. Lei, C. Chen, X. Liu, J. Chen, *Journal of the American Chemical Society* **2016**, *138*, 12894.

[28] D. Deckenbach, J. J. Schneider, *Journal of Power Sources* **2021**, *488*, 229393.

[29] W. Sun, F. Wang, B. Zhang, M. Zhang, V. Küpers, X. Ji, C. Theile, P. Bieker, K. Xu, C. Wang, M. Winter, *Science (New York, N.Y.)* **2021**, *371*, 46.

[30] J. F. Parker, J. S. Ko, D. R. Rolison, J. W. Long, *Joule* **2018**, *2*, 2519.